Hockaday, L., McKechnie, T., von Puttkamer, M.N., Lubkoll, M., 2020. The Impact of Solar Resource Characteristics on Solar Thermal Pre-heating of Manganese Ores, in: Chen, X., Zhong, Y., Zhang, L., Howarter, J.A., Baba, A.A., Wang, C., Sun, Z., Zhang, M., Olivetti, E., Luo, A., Powell, A. (Eds.), Energy Technology 2020: Recycling, Carbon Dioxide Management, and Other Technologies, The Minerals, Metals & Materials Series. Springer International Publishing, Cham, pp. 3-13. https://doi.org/10.1007/978-3-030-36830-2_1

The Impact of Solar Resource Characteritics on Solar Thermal Preheating of Manganese Ores

Lina Hockaday, Tristan McKechnie, Martina Neises von Puttkamer and Matti Lubkoll

Abstract The proposed paper evaluates an alternative ferromanganese production flowsheet seeking to preheat manganese ores with concentrating solar thermal energy to 600°C. The benefits of solar thermal preheating will be evaluated based on a cost discounted economic model taking into account the variability of the solar resource, capital costs and operating costs of a solar thermal plant over the lifetime of the project. Solar variability will be discussed based on possible implementation sites for such technologies and the cost and benefits of thermal storage in the flowsheet will also be evaluated. This work is part of the PreMa project, aiming to advance novel energy systems in the drying and preheating of furnace materials. The PreMa project has received funding from the European Union's Horizon 2020 Research and Innovation Programme under Grant Agreement No 820561.

1 Introduction

Manganese is an important additive to steel. Manganese content in steel improves toughness and wear resistance of steel and on average about 0.8% manganese is added

Lina Hockaday
Mintek, 200 Malibongwe Drive, Praegville, Randburg, 2094, Randburg, South Africa e-mail: LinaH@mintek.co.za

Tristan McKechnie
Solar Thermal Energy Research Group (STERG), Stellenbosch 7600, South Africa e-mail: 18976697@sun.ac.za

Martina Neises von Puttkamer
Institute of Solar Research, German Aerospace Center (DLR), Pfaffenwaldring 38-40, 70569 Stuttgart, Germany e-mail: Martina.Neises@dlr.de

Matti Lubkoll
Solar Thermal Energy Research Group (STERG), Stellenbosch 7600, South Africa e-mail: matti@sun.ac.za

to steel. 90% of manganese is used as steel additive in the form of ferromanganese alloys. Ferromanganese alloys are produced in either blast furnaces or electric arc furnaces with carbon as reductant. Detailed description of manganese ferroalloy production, both for high carbon ferromanganese and low carbon silicomanganese alloys can be found in literature (International Manganese Institute, 2019; Sverre E. Olsen and Lindstad, 2007). Global manganese ore mine production is summarized in Table 1 as adapted from U.S. Geological Survey (2019). The Republic of South Africa (RSA) is the leading producer of manganese ores and has the largest land based manganese ore reserves.

Table 1 Global mine production and reserves of manganese ores by country, manganese content

Year	Unit	RSA	Ukraine	Brazil	Australia	Gabon	China	Other	World Total
2017	kt/a	5 400	735	1 160	2 820	2 190	1 700	1 278	17 300
2018	kt/a	5 500	740	1 200	3 100	2 300	1 800	1 342	18 000
Reserves	kt	230 000	140 000	110 000	99 000	65 000	54 000	62 000	760 000

Global manganese ferroalloy production which include different grades of ferromanganese and silicomanganese is given in Table 2 as adapted from International Manganese Institute (2013).

Table 2 Manganese ferroalloy production by country, based on manganese content. China was the largest manganese ferroalloy producer, with production being four times more than India and ten times more than South Africa. Norway and Spain were the largest European producers of manganese ferroalloys.

Country	Production (000 mt)
China	10 349
India	2 372
RSA	741
Ukraine	713
South Korea	686
Norway	608
Japan	483
Russia	352
Australia	254
Spain	243
Other	1 447
World Total	18 249

The PREMA project (Ringdalen, 2019) aims to investigate the optimal preheating option for a high carbon ferromanganese furnace in order to reduce electricity consumption and greenhouse gas emission from manganese ferroalloy production (Haque and Norgate, 2013). Although the project also investigates pre-heating with furnace off-gas, bio- carbon and fossil carbon, this paper focuses on the novel use of concentrating solar thermal energy as the energy source for pre-heating. The cost of using concentrating solar thermal process heat is dependent on the available solar resource at the location it is captured, as well as the technology choices selected. This paper studies three possible locations for concentrating solar thermal plants

in proximity to current manganese ferroalloy smelters, as well as one location near manganese ore mines. It was attempted to select locations with existing smelters and good solar radiation in Europe, Africa and China. The locations selected for evaluation are listed below. These locations were not selected as ideal sites, for example China has locations with better solar resources in the Inner Mongolia Province, but are evaluated to provide insight into the factors involved in application of solar thermal process energy to a high temperature industrial process.

- Jiayuguan, Gansu Province, China
- Huesca, Spain
- Hotazel, Northern Cape Province, South Africa (RSA 1)
- Emalahleni, Mpumalanga Province, South Africa (RSA 2)

2 Manganese ferroalloy production process modeling

To investigate the energy demand for preheating of manganese ores, a HSC model (Outotec, 2019a,b), Version 9.9.2.3, was constructed for the PReMA project. The HSC model is based on the possible reactions that can take place during pre-heating and smelting and the extent they progress towards completion.

Traditional pre-heating systems rely on fossil fuel combustion and a reducing atmosphere with low partial pressures of oxygen is generally practiced (Tangstad et al, 2015). The novel solar thermal preheating unit relies on heated air, maintaining a oxidative atmosphere in the unit and therefore the reactions differ from those expected in a reducing atmosphere and are given in equations 1 to 8. Equation 7 is the Boudouard reaction where carbon dioxide reacts with carbon to form carbon monoxide. This reaction is likely to start taking place at temperatures above 500°C and to proceed fully only at temperatures above 800°C. Similarly, this preliminary investigation has been guided by calculated equilibrium reactions for the thermal decomposition of MnO_2 to Mn_2O_3 as published by Sverre E. Olsen and Lindstad (2007, p. 74). Future work will involve the determination of kinetics for these reactions. The completion of these reactions will influence the final energy demand of the pre-heater and values in Table. 3 are for illustrative purposes only.

The results from process modeling for pre-heating to 600°C is shown in Table 3. The process CO_2 emission factor of 2.31 is a reduction of 7% on the emissions factor for a process not employing preheating. The energy demand for a pre-heater feeding a 30MW high carbon ferromanganese furnace that requires a manganese ore feed of approximately 40t/h will therefore have an energy demand of 13.6MW to achieve a product temperature of 600°C. Due to the variable nature of the solar resource, a solar thermal plant will only be able to meet this demand in part. The following section describes the methodology to size a solar thermal plant, with thermal storage to improve availability and electrical heating as back-up for the four different locations identified as possible sites. Electrical heating was chosen as back-up technology due to the increase in zero emission electricity options available

to industry (Philibert, 2017). Using electricity as back-up rather than a fossil fuel also prevents pre-heating cycling between an oxidizing and a reducing environment, which may lead to problems with control of the carbon balance in the submerged arc furnace,(SAF).

$$MgCO_3 \longrightarrow MgO + CO_2(g) \quad (1)$$

$$CaMg(CO_3)_2 \longrightarrow MgO + CaCO_3 + CO_2(g) \quad (2)$$

$$H_2O(l) \longrightarrow H_2O\ (g) \quad (3)$$

$$2FeO \cdot OH \longrightarrow Fe_2O_3 + H_2O(g) \quad (4)$$

$$MnCO_3 \longrightarrow MnO + CO_2(g) \quad (5)$$

$$2AlO(OH) \longrightarrow Al_2O_3 + H_2O\ (g) \quad (6)$$

$$C + CO_2(g) \longrightarrow CO_2(g) \quad (7)$$

$$4\,MnO_2 \longrightarrow 2\,Mn_2O_3 + O_2\ (g) \quad (8)$$

Table 3 Illustrative modeling assumptions and resulting energy demand for the pre-heater

Reaction	1	2	3	4	5	6	7	8
Completion, %	100	80	100	100	100	100	0	100
Preheating target, °C						600		
Preheater energy demand, kWh/t feed						339.8		
Process CO_2 emission factor, t/t alloy						2.31		

3 Solar thermal plant modeling methodology

In recent years, solar thermal technology has advanced through the development of sold particle receivers (Gallo et al, 2016; Gobereit et al, 2015). Solid particle receivers operate with the solid particles directly exposed to the concentrating solar flux. The layer of solid particles in the Centrec® receiver shields the rotating structure of the receiver and make possible particle temperatures in excess of 900°C (Amsbeck et al, 2018). Figure 1 shows a schematic of a CST plant that would provide high temperature process heat to an industrial process as envisaged in the PReMA project (Ringdalen, 2019).

The purpose of this section is to compare the effect of solar resource variability on the potential for incorporating concentrating solar thermal (CST) technologies in manganese ore pre-heating. The integration of CST technologies are envisioned to lead to lower energy costs and significant reductions in carbon emissions, as already presented in Section 2. The CST plant model assumes the German Aerospace Center's (DLR) particle receiver technology (Amsbeck et al, 2018), CentRec®, for receiver and thermal energy storage. For the purpose of this assessment their receiver sizing and performance characteristics are based on Amsbeck et al (2014). The model

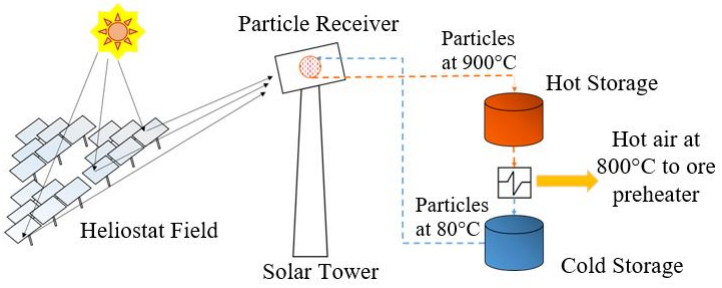

Fig. 1 Concentrating solar thermal technologies.

follows Lubkoll et al (2018) with the thermal receiver size fixed at 1 m^2 and 2.5 MW_t output. The solar field is then sized to provided a system output of 2.5 MW_t at solar equinox. Each such CST tower system can then at best provide 2.5 MW_t peak to a consumer. Multiple CST towers are foreseen to be deployed when heat demand exceeds the supply of one tower. The lowest levelized cost of heat, LCOH, of a CST system is usually found with the solar components being significantly over-sized compared to the thermal demand. This over-sizing permits thermal storage and is expressed through the solar multiple, defined as:

$$\mathrm{SM} = \frac{Q_{\mathrm{rec}}}{Q_{\mathrm{process}}}, \tag{9}$$

where Q_{rec} is the thermal output of the receiver at the solar field design point and Q_{process} is the thermal output to process.

The solar plant annual performance assessment is conducted by modeling at hourly steady state conditions . The solar resource data is obtained as typical meteorological year (TMY) from Meteonorm (Meteonorm, 2019), Version 7.3. Details regarding the plant and economic modeling, and model inputs are explained further in the paper of Lubkoll et al (2018). The solar plant operation was simulated to determine the energy produced, from which the LCOH was determined. A parametric study was then performed to determine the most suitable solar plant configuration to obtain the lowest LCOH for each site.

3.1 Field layout

The positioning of the tower within the heliostat field was investigated, resulting in an improved optical efficiency for the solar field. This is an improvement on the methodology described by Lubkoll et al (2018). The receiver is modeled angled downward 45° from the horizontal. This allows heliostats placed behind the tower have to line of sight to the receiver opening. Heliostats placed near and behind the tower have improved optical efficiency compared to heliostats in front of the tower

but further away. The optimal placement of the tower within the field was determined as presented in Figure 2. Figure 3 shows the resulting field optical efficiency. It can be seen that the tower placed at $0.6 \times r_{field}$ from the center of the field resulted in the maximum field optical efficiency. These results agree with those of Hallberg and Hallme (2018). All fields sized in this paper will therefore have a layout similar to Figure 2(c). The specification of the heliostat field now allows the capacity factor (CF) to be calculated. The capacity factor is defined as the average annual energy production divided by the process heat demand.

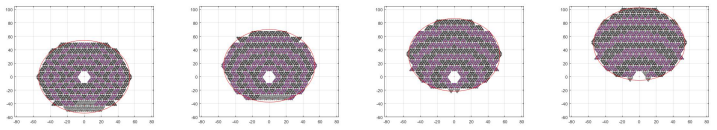

(a) Tower at center (b) Tower at 30% (c) Tower at 60% (d) Tower at 90%

Fig. 2 Tower position optimization.

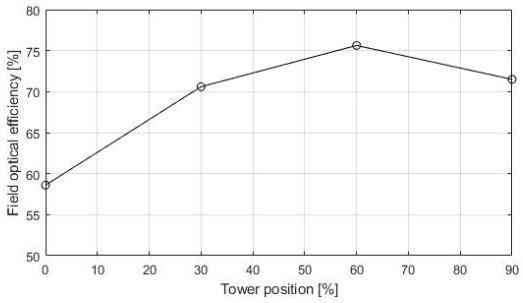

Fig. 3 Tower position within field and resulting field optical efficiency.

3.2 Operating strategy

The configuration of a CST plant producing heat at the lowest levelized cost of heat, LCOH, does not typically have a 100% capacity factor, for this reason back-up electric heaters are included as auxiliary heating for when solar heat is insufficient to meet demand. LCOH is determined by dividing the total costs over the project lifetime by the total amount of energy supplied over the lifetime of the project. A combined LCOH of solar-electric heating was calculated to determine the configuration of the solar plant that results in the lowest produced combined solar-electric heat. The cost of electrically generated heat is simplified as the cost per MWh of electricity. The combined solar-electric LCOH was calculated as:

$$\mathrm{LCOH_{comb}} = \frac{\mathrm{LCOH_{CST}Q_{CST}} + \mathrm{LCOH_{el}Q_{el}}}{\mathrm{Q_{tot}}}, \tag{10}$$

where $\mathrm{Q_{CST}}$ is the total annual solar generated heat, $\mathrm{Q_{el}}$ is the total annual electrical generated heat, $\mathrm{Q_{tot}}$ is the total annual generated heat, $\mathrm{LCOH_{CST}}$ is the cost of solar generated heat and $\mathrm{LCOH_{el}}$ is the cost of electrically generated heat.

The operating strategy for the plant is to deliver the thermal demand whenever the receiver and/or TES has sufficient energy available. At any point when the solar plant does not output the rated thermal demand then electric heating is supplemented.

4 Locations

Table 4 shows the locations that were assessed and the common solar plant parameters with DNI data from SolarGIS (2019) and solar plant specifications as modeled by Lubkoll et al (2018). The two South African locations have similar latitudes, but differ in the available solar resource. Likewise for the Chinese and Spanish locations. The solar plant specifications listed are; h_{tower} tower height, a_{rec} receiver aperture area, α the receiver tilt angle from the horizontal and η_{rec} the receiver solar to particle efficiency.

Table 4 Plant locations and resulting solar fields.

location		units	RSA 1	RSA 2	Spain	China
site data	latitude	-	27.240 S	25.886 S	41.926 N	39.897 N
	longitude	-	22.902 E	29.123 E	0.183 E	98.318 E
	DNI	kWh/(m^{2}a)	2795	2117	1929	1520
solar plant specifications	h_{tower}	m	40			
	a_{rec}	m^2	1			
	α	°	45			
	η_{rec}	%	90			

5 Results and discussion

Table 5 summarizes the results from the solar plant modeling and parametric studies. The CST parameters are configured for the lowest annual combined LCOH, incorporating solar with electric back-up for constant heat production. $\mathrm{LCOH_{CST,pot}}$ represents an optimized CST only plant configuration and provides reference of the lowest possible solar LCOH. Relative to this, the configuration represented by $\mathrm{LCOH_{CST}}$ have significantly higher solar capacity factor to reduce the $\mathrm{LCOH_{comb}}$ by suppressing electricity usage. The economic benefit of increasing the solar capacity

factor is more than the added cost for a larger CST systems. This is because for all locations CST heat is more affordable than electrical heat.

Locations with similar latitudes (RSA 1 and RSA 2, and Spain and China) experience similar sun angles throughout the year. As the solar fields are sized for all locations with a common design point DNI, the locations with similar latitudes therefore have similar sized fields. Further, the annual solar field efficiency can be seen to have increased compared to the results from Lubkoll et al (2018), as the tower has been located at an improved location.

The Spanish and Chinese locations can be seen to have significantly more expensive electricity and therefore favor systems with higher SM and TES size, thereby off-setting the amount of electricity required. Even then, the Chinese location shows relatively moderate CF due to the poor direct normal irradiance (DNI). The South African locations feature less storage, nonetheless show high CF due to high solar resources. RSA 1 is able to achieve a high capacity factor as the solar resource for the location is excellent. RSA 2's solar plant configuration is not further over-sized as the electricity cost is relatively low.

Table 5 Solar plant configuration.

Type	Parameters	Units	RSA 1	RSA 2	Spain	China
Site data:	DNI	kWh/(m^{2}a)	2795	2117	1929	1520
	$LCOH_{el}$	\$/MWh	47.29	47.29	115.51	74.65
CST potential:	$LCOH_{CST,pot}$	\$/MWh	35.48	43.43	46.28	56.02
Combined system, per tower:	TES	h	14	14	22	16
	A_{sf}	m^2	3563	3563	3616	3616
	$\eta_{sf,a}$	%	65	66	62	62
	SM	-	3.2	3.0	4.5	4.2
	$\dot{Q}_{process}$	MW	0.79	0.82	0.55	0.60
	CF_{CST}	%	79	63	76	63
	$LCOH_{CST}$	\$/MWh	36.25	43.85	54.02	57.46
	$LCOH_{comb}$	\$/MWh	38.55	45.13	68.98	63.75
For pre-heater integration:	Number of towers	-	18	17	28	23
	Total heliostat field area	ha	6.4	6.1	9.1	8.3
Benefit vs. total electrification	$\Delta LCOH$[4)]	%	19	5	40	17

[4)] $\Delta LCOH = (LCOH_{el} - LCOH_{comb})/LCOH_{el}$

All locations benefit from incorporating CST technologies. The higher the electricity tariff for a location, the larger the solar system will be to suppress electricity use. The benefit of the solar with electric back-up compared to total electrification is shown in the final row of Table 5. Electricity cost data for South Africa was obtained from ESKOM (2019), for Spain from International Energy Agency (2018) and for China from China Briefing News (2019). The benefit of solar thermal heating as compared to electrification is of course larger for countries with higher electricity costs such as Spain. It should be noted that the cost savings will increase with electrical tariff increases, whereas the solar heat cost will remain steady over the life of the system. The model in this paper does not include electricity price escalation.

6 Conclusion

This paper evaluated the energy demand for a pre-heater driven by a solar thermal plant providing hot air and backed up by electric heating elements. The aim of the study was to investigate the feasibility of high temperature solar thermal process heat for preheating as a cost effective alternative to electrification of the process as a way of limiting green house gas emissions. The results confirmed that the combined solar thermal and electric heating produced lower energy costs over a project lifetime of 25 years compared to heating through electrification only for all locations evaluated. Locations with a high annual DNI had lower levelized energy costs than locations with lower annual DNI levels, but the cost of electricity at each location also had an influence on the solar thermal plant design. High electricity costs increased the amount of thermal energy storage and the solar multiple to ensure that the most cost effective solution has a high solar share. Countries with high annual DNI and low electricity costs may in future have a global competitive advantage for low emission, high temperature process energy applications.

The methodoloy was optimised for heliostat field size, tower position, solar multiple (SM) and thermal energy storage (TES) at each location. The optimization resulted in higher capacity factors than previously published (Lubkoll et al, 2018) for systems that were not optimized to achieve the lowest LCOH.

In conclusion, although combustion heating with fossil fuels such as metallurgical coke and coal remain the least cost alternative at the time of writing, solar thermal process energy can compete favorably with process heating by electrification for projects with a lifetime of 25 years. With industry targets of lowering greenhouse gas emissions becoming more urgent (Philibert, 2017), evaluating where solar thermal process energy can be a cost effective alternative is of relevance to industry.

Acknowledgements

The PReMA project has received funding from the European Union's Horizon 2020 Research and Innovation Programme under Grant Agreement No 820561. This paper is published with the permission of Mintek.

References

Amsbeck L, Behrendt B, Prosin T, Buck R (2014) Particle tower system with direct absorption centrifugal receiver for high temperature process heat. In: Energy Procedia 00 (2015) 000–000, Elsevier, Beijing, China

Amsbeck L, Buck R, Ebert M, Gobereit B, Hertel J, Jensch A, Rheinländer J, Trebing D, Uhlig R (2018) First tests of a centrifugal particle receiver with a 1m2 aperture.

In: AIP Conference Proceedings, AIP Publishing, Santiago, Chile, vol 2033, DOI 10.1063/1.5067040, URL http://aip.scitation.org/doi/abs/10.1063/1.5067040

China Briefing News (2019) China Electricity Prices for Industrial Consumers: A Guide for Investors. URL https://www.china-briefing.com/news/china-electricity-prices-industrial-consumers/

ESKOM (2019) 2019/20 Tariffs and charges. URL http://www.eskom.co.za/CustomerCare/TariffsAndCharges/Pages/Tariffs_And_Charges.aspx

Gallo A, Roldán MI, Alonso E, Fuentealba E (2016) Considerations for Using Solar Rotary Kilns for High Temperature Industrial Processes with and Without Thermal Storage. In: Proceedings of EuroSun2016, International Solar Energy Society, Palma de Mallorca, Spain, pp 1–10, DOI 10.18086/eurosun.2016.02.04, URL http://proceedings.ises.org/citation?doi=eurosun.2016.02.04

Gobereit B, Amsbeck L, Buck R, Pitz-Paal R, Röger M, Müller-Steinhagen H (2015) Assessment of a falling solid particle receiver with numerical simulation. Solar Energy 115:505–517, DOI 10.1016/j.solener.2015.03.013, URL https://linkinghub.elsevier.com/retrieve/pii/S0038092X15001310

Hallberg M, Hallme E (2018) Introducing a central receiver system for industrial high-temperature process heat applications. PhD thesis, KTH ROYAL INSTITUTE OF TECHNOLOGY, Stockholm, Sweden, URL http://www.diva-portal.org/smash/get/diva2:1303784/FULLTEXT01.pdf

Haque N, Norgate T (2013) Estimation of greenhouse gas emissions from ferroalloy production using life cycle assessment with particular reference to Australia. Journal of Cleaner Production 39:220–230, DOI 10.1016/j.jclepro.2012.08.010, URL https://linkinghub.elsevier.com/retrieve/pii/S0959652612004179

International Energy Agency (2018) Key world energy statistics. URL https://www.iea.org/statistics/kwes/prices/

International Manganese Institute (2013) 2013 IMnI Public Report. URL http://www.manganese.org/files/publications/PUBLIC%20RESEARCH%20REPORTS/2013_IMnI_Public_Report.pdf

International Manganese Institute (2019) About Manganese. URL http://www.manganese.org/about-manganese/

Lubkoll M, Hockaday SAC, Harms TM (2018) Integrating Solar Process Heat into Manganese Ore Pre-Heating. Durban, p 8, URL https://www.sasec.org.za/full_papers/57.pdf

Meteonorm (2019) Intro - Meteonorm (de). URL https://meteonorm.com/en/

Outotec (2019a) HSC Chemistry. URL https://www.outotec.com/products/digital-solutions/hsc-chemistry/

Outotec (2019b) HSC Sim – Process Simulation Module. URL https://www.outotec.com/products/digital-solutions/hsc-chemistry/hsc-sim-process-simulation-module/

Philibert C (2017) Renewable Energy for Industry. Tech. rep., URL https://www.iea.org/publications/insights/insightpublications/Renewable_Energy_for_Industry.pdf

Ringdalen E (2019) What is PREMA? URL https://www.spire2030.eu/prema

SolarGIS (2019) iMaps. URL https://solargis.com/maps-and-gis-data/overview/

Sverre E Olsen MT, Lindstad T (2007) Production of Manganese Ferroalloys. tapir academic press

Tangstad M, Ichihara K, Ringdalen E (2015) Pretreatment Unit in Ferromanganese Production. In: The Fourteenth International Ferroalloys Congress, INFACON, Kiev, Ukraine, pp 99–106, URL https://www.pyrometallurgy.co.za/InfaconXIV/099-Tangstad.pdf

US Geological Survey (2019) Mineral Commodity Summaries 2019: U.S. Geological Survey, URL https://doi.org/10.3133/70202434